On the Accuracy and Efficiency of Split-Field, Uniaxial, and CFS Perfectly Matched Layers

Chicheng Xu, Paul Tsuji, and Kristen Parrish

***Abstract*—The 2-D TMz field equations are formulated and implemented in the split-field PML, uniaxial anisotropic PML, and complex frequency shifted PML using the FDTD method. In various numerical experiments, computational settings were varied to study the accuracy of the three PML techniques, using a simple 2-D vacuum problem. The FDTD implementations were first validated by comparing with the analytical solution of a time-harmonic source. All numerical results were then compared to a large reference field to calculate the reflection error. The experiments verified that split-field and uniaxial PML have the same effectiveness in absorbing incident waves, with the uniaxial PML being more computationally efficient. It was also shown that the complex frequency shifted PML can achieve the same efficiency as uniaxial PML. However, both theoretical analysis and experimental results indicate that complex frequency shifted PML is not applicable to a 2-D TMz problem.**

I. Introduction

PERFECTLY matched layers (PMLs) are employed in the finite difference time domain (FDTD) method to absorb incident waves without reflections, truncating the computational region needed for simulations. Since the introduction of the split-field PML technique by Berenger in 1994 [1], many researchers have worked to improve upon this original method. The uniaxial PML was introduced in 1995 [2] by Sacks, et. al by implementing permittivity and permeability as tensors in Maxwell's equations, instead of modifying Maxwell's equations. It was shown that this PML method is mathematically equivalent to the original split-field PML [3]. The CFS PML was introduced in 1996 by Kuzuoglu and Mittra [4]. This method was introduced in order to force the PML equations to be causal, by forcing the constitutive parameters to satisfy the Kramers-Kronig relationships. The CFS PML has been verified to effectively reduce the reflections in late time or with elongated grids. In this paper, the three methods are compared by applying them to an FDTD simulation of a current in free space.

II. Formulation

A. Problem statement

An infinite z-directed current source is radiating in free space. The current source is suspended in free space as shown in Figure 1. Maxwell's equations are solved in a vacuum medium and the electric and magnetic fields radiating from the current are calculated. Since there is no variation in the z direction and there is no magnetic current, E_x = E_y = H_z = 0; the 2-D TMz equations are

$$\frac{\partial H_x}{\partial y} - \frac{\partial H_y}{\partial x} = j\omega\varepsilon E_z \tag{1}$$

$$-\frac{\partial E_z}{\partial y} = j\omega\mu H_x \tag{2}$$

$$\frac{\partial E_z}{\partial x} = j\omega\mu H_y \tag{3}$$

where ε is the permittivity and μ is the permeability of the simulated space.

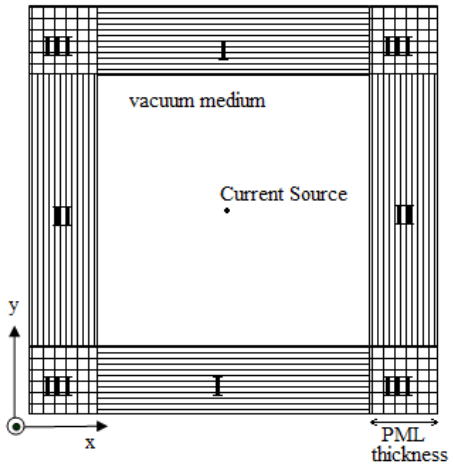

Fig. 1. Cross-sectional view of simulated problem. The three PML regions are indicated I, II and III.

The three PML regions that surround the free space medium are shown in Figure 1. In these regions, electromagnetic waves do not necessarily follow Maxwell's equations, but instead follow split-field or stretched equations, as derived by Berenger [1], Chew [5] et. al.

B. Split-field PML

The PML equations were derived from Berenger's equations [1], reproduced below. The discretized equations are included in Appendix 1. The split-field FDTD grid, based on Yee's grid [6], is shown in Figure 2.

$$\varepsilon\frac{\partial E_{zx}}{\partial t} + \sigma_x E_{zx} = \frac{\partial H_y}{\partial x} \tag{4}$$

$$\varepsilon\frac{\partial E_{zy}}{\partial t} + \sigma_y E_{zy} = -\frac{\partial H_x}{\partial y} \tag{5}$$

$$\mu\frac{\partial H_x}{\partial t} + \sigma_x^* H_x = -\frac{\partial E_{zx} + E_{zy}}{\partial y} \tag{6}$$

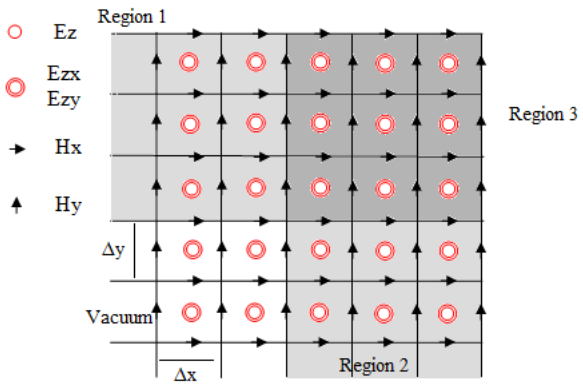

Fig. 2. Top-right corner of FDTD grid for split-field PML.

$$\mu\frac{\partial H_y}{\partial t} + \sigma_y^* H_y = \frac{\partial E_{zx} + E_{zy}}{\partial x} \tag{7}$$

The electric conductivities of the PML are defined as σ_x and σ_y, while the magnetic conductivities are $\sigma_x{}^*$ and $\sigma_y{}^*$. H_x and H_y are the magnetic fields in the PML, and E_{zx} and E_{zy} are Berenger's electric fields (E_{zx} + E_{zy} = E_z). Equations (4) - (7) are implemented over the regions I, II and III - in the vacuum, Mawell's equations are discretized and implemented. In region I, $\sigma_x = \sigma_x^* = 0$, and in region II, $\sigma_y = \sigma_y^* = 0$. In region III, σ_x and σ_y are defined as above, with $\sigma_x/\varepsilon = \sigma_x^*/\mu$ and $\sigma_y/\varepsilon = \sigma_y^*/\mu$. These matching conditions must be satisfied in order to eliminate reflections.

C. Uniaxial PML

The FDTD update equations are derived from Maxwell's equations for a stretched, anisotropic medium, as described in [3]. In the vacuum region, Maxwell's equations were implemented, while in the three distinct PML regions, equations (8) - (10) were used. The implemented update equations are included in Appendix 2; these are similar to those derived in [3]. The values of σ_x and σ_y are defined the same as for the split-field PML. The grid used is shown in Figure 3.

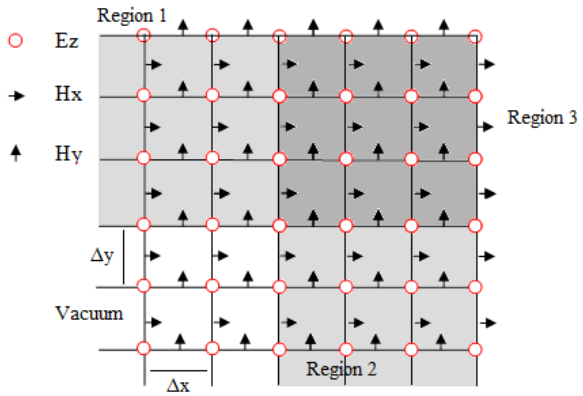

Fig. 3. Top-right corner of FDTD grid for uniaxial PML.

$$\frac{\partial H_x}{\partial y} - \frac{\partial H_y}{\partial x} = j\omega\varepsilon(1 + \frac{\sigma_x}{j\omega\varepsilon_0})(1 + \frac{\sigma_y}{j\omega\varepsilon_0})E_z \tag{8}$$

$$-\frac{\partial E_z}{\partial y} = j\omega\mu\frac{1 + \frac{\sigma_y}{j\omega\varepsilon_0}}{1 + \frac{\sigma_x}{j\omega\varepsilon_0}}H_x \tag{9}$$

$$\frac{\partial E_z}{\partial x} = j\omega\mu\frac{1 + \frac{\sigma_x}{j\omega\varepsilon_0}}{1 + \frac{\sigma_y}{j\omega\varepsilon_0}}H_y \tag{10}$$

D. CFS PML

Because the CFS PML is similar to the uniaxial, in that both make use of stretched coordinates (as opposed to the split-field formulation), the grid shown in Figure 3 was used. The update equations for the CFS PML are derived from Maxwell's stretched equations, as in [5]. The implemented update equations are included in Appendix 3; these are similar to those derived in [7].

$$\frac{1}{s_x}\frac{\partial H_x}{\partial y} - \frac{1}{s_x}\frac{\partial H_y}{\partial x} = j\omega\varepsilon E_z \tag{11}$$

$$-\frac{1}{s_y}\frac{\partial E_z}{\partial y} = j\omega\mu H_x \tag{12}$$

$$\frac{1}{s_x}\frac{\partial E_z}{\partial x} = j\omega\mu H_y \tag{13}$$

$$s_x = \kappa_y + \frac{\sigma_x}{\alpha_x + j\omega\varepsilon_0} \tag{14}$$

$$s_y = \kappa_y + \frac{\sigma_y}{\alpha_y + j\omega\varepsilon_0} \tag{15}$$

The same σ profiles that were used in the uniaxial and split-field implementations were used with the CFS implementation. The coefficients s_x and s_y are defined to stretch the fields in the PML, forcing it to behave as an anisotropic medium. The parameters κ_x, κ_y, α_x, α_y are characteristics of the CFS that are frequency dependent, used to shift the pole of the stretching constant so that the PML is causal.

III. Numerical Results

The FDTD method is used to solve Maxwell's equations iteratively across a grid, then iterating the time step Δt. First, the results of the FDTD method were validated by comparing to an analytical solution. Next, the performance of the Split-field, Uniaxial, and CFS PMLs were tested. Several experiments were then performed in order to develop greater understanding on how the characteristics of each PML affect performance. Finally, the computational efficiencies of each method were analyzed.

A. Verification of FDTD Implementation

In order to validate the code and show that it produces the correct results, a canonical problem with an analytical solution was chosen first. The radiation from an infinite line time-harmonic current source of single frequency is a standard problem and can be found in many electromagnetics textbooks [8]. For the TMz mode, the analytical solution of the electric field in the frequency domain is

$$E_z = -I_e\frac{\beta^2}{4\omega\varepsilon}H_0^{(2)}(\beta\rho) \tag{16}$$

where I_e is the amplitude of the source, $\beta = \omega\sqrt{\mu\varepsilon}$ is the wavenumber, ρ is the distance from the source, and $H_0^{(2)}(\beta\rho)$ is the zero order Hankel function of the second kind evaluated at $(\beta\rho)$. Two important points must be noted: first, implementing the source in the time domain requires a gradual amplitude increase starting from 0, rather than a sudden excitation. If the source is immediately introduced to the system, unwanted high-frequency components become apparent, and the result is a slightly distorted waveform. Thus, the source J_z used is of the form

$$J_z = I_e(1 - e^{-(t/d)})cos(\omega t) \tag{17}$$

where d is some constant which slows the rate of increase; in the experiments presented, d=20Δt. Secondly, to properly compare the analytical solution with the numerical results, phasor notation must be used to transform the solution into the time domain; that is, the real part of the data produced by equation (16) must be taken after being multiplied with $e^{j\omega t}$. A plot of all three solutions (analytical, uniaxial and split-field) are shown in Figure 4.

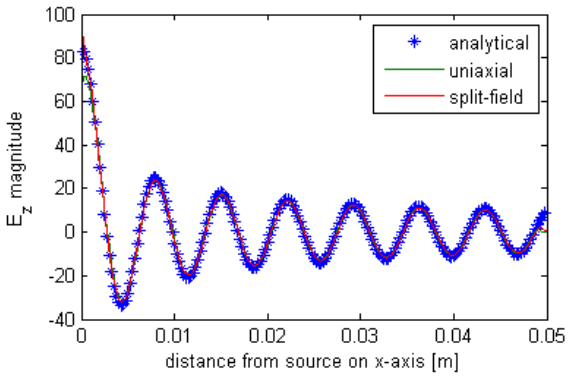

Fig. 4. Electric Field of all three as a function of distance from the current source, at 400Δt.

To gauge the accuracy of the results, the relative error 2-norm was used. If $E_{numerical}$ is the vector of E-field values produced by the FDTD code and $E_{analytical}$ is the vector of E-field values produced by equation (16) at the same grid points, the relative error 2-norm can be computed by the following expression:

$$\left(\frac{||E_{analytical} - E_{numerical}||_2}{||E_{analytical}||_2}\right) \tag{18}$$

For the 10cm by 10cm square discretized into a 400x400 mesh, the relative error 2-norms for fields along the x-axis were computed for times after the steady state was reached, i.e. after the wave reaches the boundary and reflection begins. Because the fields decay exponentially in the PML, the error norms were computed without these elements in the vector, as it would introduce fictitious errors that would otherwise not exist if the PML was also a vacuum region. The results of this error calculation are shown in Figure 5.

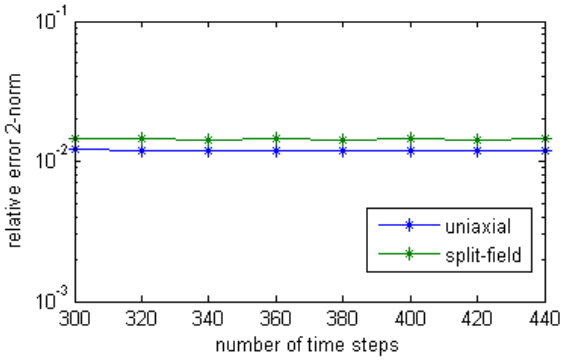

Fig. 5. Calculated relative error 2-norms for the split-field and uniaxial FDTD implementations in the vacuum region.

B. Initial Settings and Reference Problem

Over the course of the experiments, several properties of the PMLs were varied. In each experiment, only one setting was varied at a time. These settings are described in this section for future reference.

The domain was 0.15 m x 0.15 m in area, 150 x 150 in cell count. This implied that Δx = Δy = 0.001. Throughout all the presented simulations, a square grid was used, so Δx and Δy are referred to as Δ. The time step used in all simulations was the optimal time step, calculated by $\Delta t = \frac{\Delta}{\sqrt{2}c} \cong 2.36$ ps, where c is the speed of light in a vacuum.

The PML thickness was 8 cells on each side. This implied that the vacuum grid is actually 134 x 134 cells. The PML conductivities, σ_x and σ_y, vary over the PML according to a polynomial. On the PML/vacuum boundary, the conductivities are equal to 0, while on the PML/PEC boundary they are at their maximum value. They are calculated as

$$\sigma_{xi} = \sigma_{max}\Delta x(\frac{i-1}{2n_{pml}})^m, i = 1...2n_{pml}+1 \tag{19}$$

$$\sigma_{y_i} = \sigma_{max}\Delta y(\frac{i-1}{2n_{pml}})^m, i = 1...2n_{pml}+1 \tag{20}$$

where n_{pml} is the thickness of the PML (here, 8 cells). Note that the these conductivities are calculated at every half-grid step, while the field vectors are calculated at alternating half-grid steps. The value of σ_{max} is 90, while the exponent m is set to 3.5.

In order to gauge the accuracy of each method, two reference problems were constructed, one based on the split-field PML, and one based on the uniaxial PML. All the characteristics of each respective reference problem are exactly the same as the appropriate PML problem being analyzed. However, in the reference problem, the free space area is increased without adjusting either the spatial or time step. The reference problem thus is a simulation of an identical electromagnetic structure in a larger free space area. This allows us to gauge how much of the field at any point on the grid is contributed by the source (the correct result), and how much is reflected by the PML (undesired reflection error). The reference problem uses a 400 x 400 cell grid (384 x 384 free space cells, 8 cell thick PML), with Δ = 0.001 and time step approximately 2.36 ps. The reflection error is then calculated

as in [7]. The equation used is

$$R = 20log_{10}\left(\frac{||E(t) - E_{ref}(t)||}{||max(E_{ref}(t))||}\right) \quad (21)$$

where $E(t)$ is the electric field generated by the PML simulation at a certain time, $E_{ref}(t)$ is the field of the corresponding reference problem at this same time. For the split-field PML, the split-field reference problem is used, while the uniaxial reference problem is used for analysis with the uniaxial and CFS PMLs.

For the following numerical tests, a Gaussian pulsed current was implemented using the following equation:

$$J = Ae^{-\frac{(t-t_0)^2}{t_w^2}} \quad (22)$$

where A is the amplitude, t_w is the width of the pulse ($20\Delta t$, where Δt is the length of the time step implemented) and t_0 is the center of the pulse ($60\Delta t$). The pulse is not centered at t = 0 in order to reduce the deletrious effects of the pulse's DC component.

C. Comparison of Three PMLs

The accuracy of the three PMLs was examined by simulating each PML with the parameters described in the previous section. Additionally, the CFS PML has parameters α_x = α_y = 0.05 (as in [7]) and κ_x and κ_y are given by

$$\kappa_x = \kappa_y = 1 + 10(\frac{i-1}{2n_{pml}})^m, i = 1...2n_{pml} + 1 \quad (23)$$

as in [9]. Each simulation was run from 0 to $350\Delta t$ in increments of $5\Delta t$. The results of this simulation are shown in Figure 6, showing the reflection error as calculated above for each PML method over time. Note that before approximately 110 time steps, the magnitude of relative error is 0, and so does not appear in the log-scale graph. Once the pulse is reflected by the boundary, error appears since the pulse sees a PML boundary instead of a vacuum. This graph shows that the uniaxial code and split-field codes do in fact give identical results after the incident wave reaches the PML boundary, when all simulation settings are the same, verifying the derivation in [3]. The figure also shows that the CFS PML exhibits very large reflection error. This is explained in a later section.

D. Experimental Results

For each experiment, the characteristics described above were used, while one characteristic was varied. Since the performance of the PML varies over time, the maximum error was calculated for time steps from 0 to 350 and the maximum value of this error over time for each grid size was used and plotted against the varied characteristic.

1) Time step: The optimal time step was scaled to show the effects of using a time step greater than or less than the optimal time step. The results of this simulation are shown in Figure **??**. With a Δt larger than Δt_{opt}, the FDTD method is unstable and produce incorrect results. With a Δt less than Δt_{opt}, a loss in performance is observed. Therefore, Δt is shown to be the optimal time step.

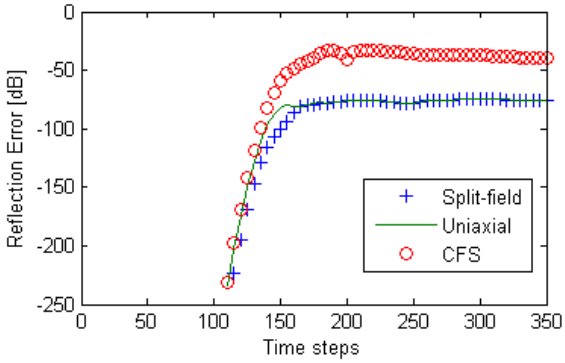

Fig. 6. Reflection error over time for the split-field, uniaxial and CFS PML implementations.

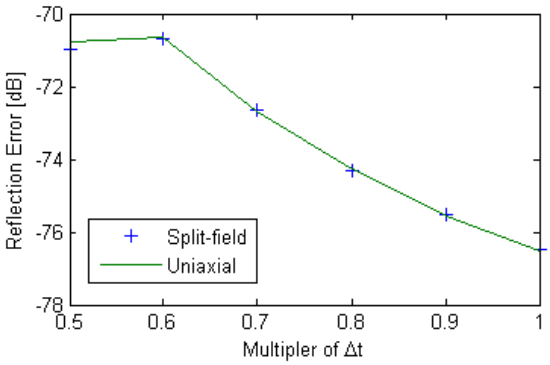

Fig. 7. Maximum reflection error for split-field and uniaxial PMLs vs. time step.

2) Grid size: Simulations were performed to determine how the accuracy was affected by the addition of more vacuum cells. In other words, the distance from the current source to the PML boundary was incremented without changing any other parameters in the simulation. With these simulations, the grid size was decreased until the error compared to the reference simulation became unreasonably large. Grid size was also increased until it was apparent that additional cells would not increase the accuracy of the simulation.

The vacuum grid size was examined at 6, 10, 14, 34, 54, 74, 104, 134, and 164 cells in order to demonstrate how accuracy is affected. The results are shown in Figure 8. At vacuum grid sizes down to approximately 50 cells, the error is still less than -60 dB. The plot also shows that performance enhancement by increasing the number of cells is limited. As the number of vacuum cells approaches approximately 120 cells, the added performance benefits by increasing the grid size are negligible.

3) Grid steps: Simulations were performed to determine how the step size (Δ) affects accuracy. Increasing the grid step decreases simulation time, but also decreases accuracy. The grid step size was increased until the error compared to the reference simulation became unreasonably large, and was decreased to show that after a certain point, there is only a small benefit to further decreasing this parameter. Simulations were performed at a grid area of constant size (0.15 m) with

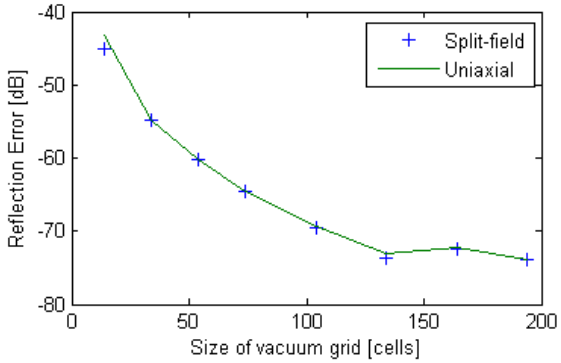

Fig. 8. Maximum reflection error for split-field and uniaxial PMLs vs. number of cells.

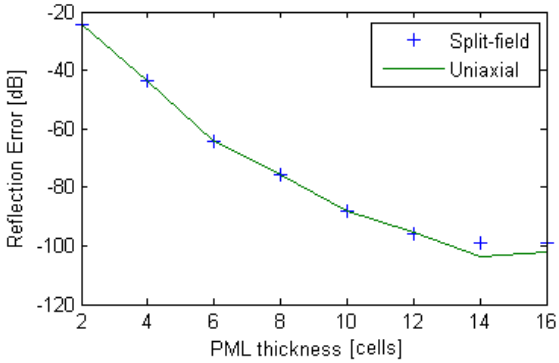

Fig. 10. Maximum reflection error for split-field and uniaxial PMLs vs. PML thickness.

Δ being 0.5, 0.6, 0.75, 1, 2, 3, 4, 5, 6, and 10 mm. The results are shown in Figure 9 - note that the x-axis is in log scale. This illustrates that at a certain point, further decreases in the step size do not improve the accuracy. It is evident that as Δ increases, the error increases. This should be expected, since increasing Δ and holding the grid constant is analogous to increasing the number of cells examined while holding Δ constant, as was explored in the previous section.

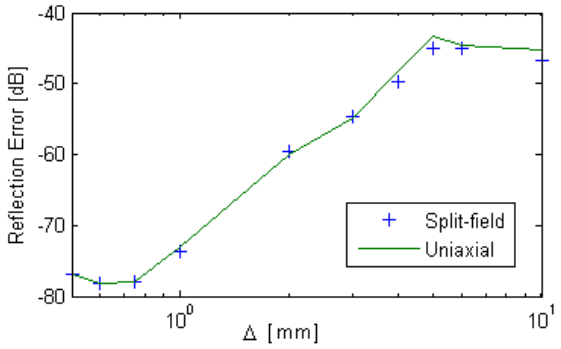

Fig. 9. Maximum reflection error for split-field and uniaxial PMLs vs. Δ.

4) PML thickness: The thickness of the PML was adjusted in order to see how large the PML should be before there is no additional increase in accuracy. The PML thickness was increased from 2 to 16 in increments of 2 cells.

The results of the error calculations for these PML thicknesses is shown in Figure 10. As PML thickness increases, the error decreases, which aligns with expectations. With less distance in the PML material between the vacuum and the PEC backing, one would expect that the field would not decay as much in the PML, which would cause higher values for reflection. The plot shows that there is a limit to the benefits of increasing the PML thickness - when the PML is 12 cells thick, the error is comparable to that with 14 and 16 cells.

5) PML profile: The two PML implementations have conductivities σ_x and σ_y. As shown previously in this paper, these values vary over the PML. In order to adjust the profiles, the exponent m can be adjusted. For both PMLs, the value m was adjusted from 1 to 6, as shown in Figure 11. This demonstrates that there is an optimal value for m. As in [3], the optimal value is close to 3.5. Also, the value σ_{max} is varied from 5 to 100. This shows that an optimal value for σ_{max} in this case is approximately 10. This is confirmed in [3], which states a theoretically derived value for σ_{max} = (m+1)/(150$\pi\Delta\sqrt{\varepsilon_r}$), with grid size and value for m calculated as 9.55.

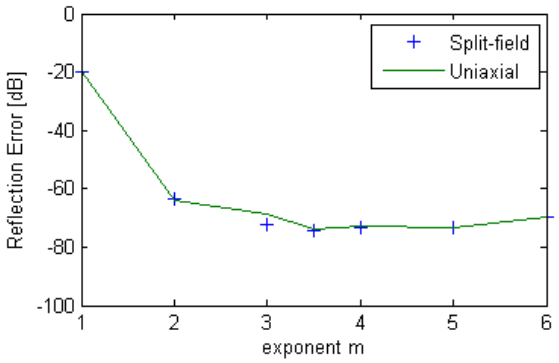

Fig. 11. Maximum reflection error for split-field and uniaxial PMLs vs. exponent m.

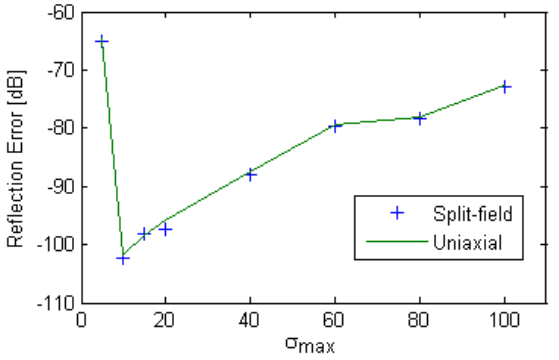

Fig. 12. Maximum reflection error for split-field and uniaxial PMLs vs. σ_{max}.

E. Comparison of PML Efficiencies

To measure the CPU time used by each method, all three methods were implemented in Fortran 90 and compiled with

the maximum optimization feature in MS Visual Studio. All programs were run on a Dell PC with 2.99 GB of RAM and an Intel CORE 2Duo CPU (2.40 GHz). Figure 13 shows the plots of CPU time vs. time steps run; the computing time in each method increases linearly with the number of time steps. The Uniaxial and CFS implementations are similar in terms of computational efficiency, and both are more computationally efficient than the split-field implementation, which has been confirmed [2].

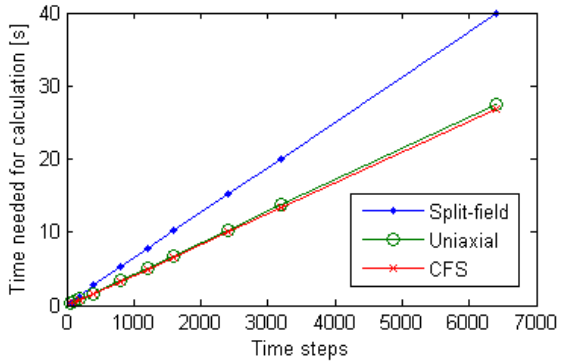

Fig. 13. Seconds per calculation for the split-field and uniaxial PML implementations.

However, by comparing the discretized equations in the three methods, we find that the difference in computing time is only caused by the PML regions, since the equations implemented for vacuum space are all the same. In the split-field implementation, the exponential function is called frequently, which is more computationally expensive than linear calculations. Additionally, it uses two arrays for the E_{zx} and E_{zy} fields, which will also cost extra time. However, the introduction of auxiliary update variables in the uniaxial and CFS methods also introduces extra computing time. With the PML thickness much less than the vacuum dimension, the efficiency for the three methods should be very close. In fact, the efficiency is highly dependent on code implementation and the nature of the problem examined.

F. Notes on CFS in 2-D

The implementation of the CFS in the 2-D TMz problem showed high reflection errors of approximately -40 dB - much larger than that exhibited by the split-field and uniaxial PMLs as shown in Figure 6. It is not an implementation error but an intrinsic defect of CFS method - it is not applicable to the 2-D problem. To see this, one can consider the field H_y in region I. With $k_x = 1.0$ and no auxilliary ψ_{hyz}, the equation for updating H_y reduces to Maxwell's equation for H_y, which means the PML in this region does not absorb H_y at all. To verify this point, we compared the cross section of the E_z field with a reference simulation (Figure 14) and the CFS PML (Figure 15). At $300\Delta t$, the field produced by the pulse is mostly dissipated, as shown in Figure 14. However, after 300 time steps, the CFS PML exhibits very high reflections. Examining sufficiently long times (observing after the field has reached the PML boundary), the reflection from regions I and II are significant.

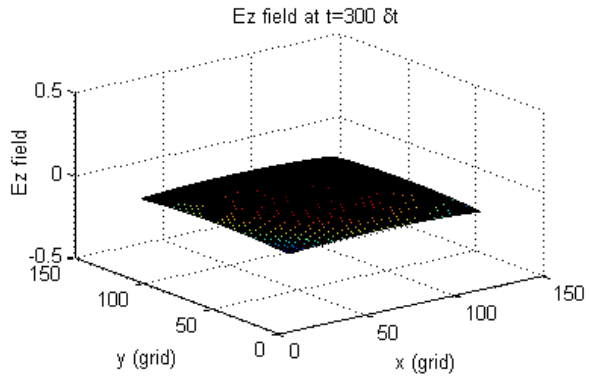

Fig. 14. Electric field observed at $300\Delta t$ with the reference uniaxial simulation.

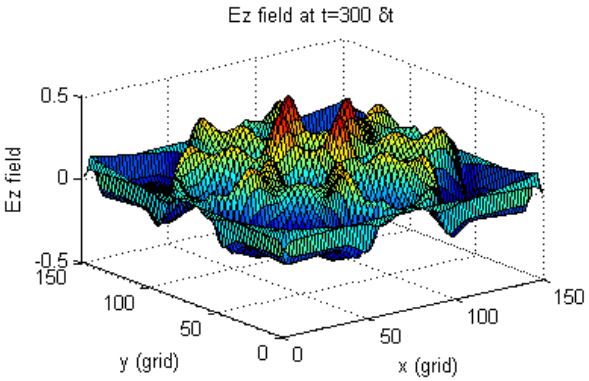

Fig. 15. Electric field observed at $300\Delta t$ with the CFS implementation.

IV. Conclusions

Three types of PML absorbing boundaries were constructed to simulate the fields radiating from an infinite current source in free space. The solutions were first validated by comparing with an analytical solution. Numerical comparisons were then made to show how the three methods differed in accuracy and computational cost, and to verify results observed in existing publications. In these studies, the split-field and uniaxial PMLs are shown to be equivalent in effectiveness of absorbing the incident waves radiated by a Gaussian pulsed current. Simulation results show that optimal PML performance can be achieved by adjusting conductivity, PML profile, size, grid size and time step. Unfortunately, the CFS PML fails in the 2-D problem due to the nature of the equations. As for efficiency, although the experimental results show that the uniaxial and CFS PMLs are better than the split-field formulation, this result is not conclusive, as computation time is highly dependent on the nature of the problem being studied and code implementation.

References

[1] J.-P. Berenger, "A perfectly matched layer for the absorption of electromagnetic waves," *J. Comput. Phys.*, vol. 114, no. 2, pp. 185–200, 1994.

[2] Z. Sacks, D. Kingsland, R. Lee, and J.-F. Lee, "A perfectly matched anisotropic absorber for use as an absorbing boundary condition," *Antennas and Propagation, IEEE Transactions on*, vol. 43, no. 12, pp. 1460–1463, Dec 1995.

[3] S. Gedney, "An anisotropic perfectly matched layer-absorbing medium for the truncation of FDTD lattices," *Antennas and*

Propagation, IEEE Transactions on, vol. 44, no. 12, pp. 1630–1639, Dec 1996.

[4] M. Kuzuoglu and R. Mittra, "Frequency dependence of the constitutive parameters of causal perfectly matched anisotropic absorbers," *Microwave and Guided Wave Letters, IEEE*, vol. 6, no. 12, pp. 447–449, Dec 1996.

[5] W. Chew and W. Weedon, "A 3d perfectly matched medium from modified maxwell's equations with stretched coordinates," *Microwave and Opt. Technology Letters, IEEE*, vol. 13, no. 7, pp. 599–604, 1994.

[6] K. Yee, "Numerical solution of inital boundary value problems involving maxwell's equations in isotropic media," *Antennas and Propagation, IEEE Transactions on*, vol. 14, no. 3, pp. 302–307, May 1966.

[7] J. A. Roden and S. D. Gedney, "Convolutional PML (CPML): An Efficient FDTD Implementation of the CFS-PML for Arbitrary Media," *Microwave and Optical Technology Letters, IEEE*, vol. 27, no. 5, Dec. 2000.

[8] C. A. Balanis, *Advanced Engineering Electromagnetics*, 3rd ed. Wiley, 1989.

[9] S. Gedney, G. Liu, J. Roden, and A. Zhu, "Perfectly matched layer media with CFS for an unconditionally stable ADI-FDTD method," *Antennas and Propagation, IEEE Transactions on*, vol. 49, no. 11, pp. 1554–1559, Nov 2001.